AGU PUBLICATIONS

Geochemistry, Geophysics, Geosystems

RESEARCH ARTICLE
10.1002/2017GC007244

Key Points:
- Microstructures of experimentally deformed bridgmanite and ferropericlase aggregates were studied orientation mapping in the TEM
- Bridgmanite deforms by localized shear deformation lamellae
- Most ferropericlase grains show strain much larger than the bulk strain of the sample without showing clear evidence for recrystallization

Supporting Information:
- Supporting Information S1
- Figure S1

Correspondence to:
P. Cordier,
patrick.cordier@univ-lille1.fr

Citation:
Nzogang, B. C., Bouquerel, J., Cordier, P., Mussi, A., Girard, J., & Karato, S. (2018). Characterization by scanning precession electron diffraction of an aggregate of bridgmanite and ferropericlase deformed at HP-HT. *Geochemistry, Geophysics, Geosystems*, *19*, 582–594. https://doi.org/10.1002/2017GC007244

Received 18 SEP 2017
Accepted 27 JAN 2018
Accepted article online 1 FEB 2018
Published online 2 MAR 2018

Characterization by Scanning Precession Electron Diffraction of an Aggregate of Bridgmanite and Ferropericlase Deformed at HP-HT

B. C. Nzogang[1], J. Bouquerel[1], P. Cordier[1], A. Mussi[1], J. Girard[2], and S. Karato[2]

[1]Univ. Lille, CNRS, INRA, ENSCL, UMR 8207-UMET-Unité Matériaux et Transformations, Lille, France, [2]Department of Geology and Geophysics, Yale University, New Haven, Connecticut, USA

Abstract Scanning precession electron diffraction is an emerging promising technique for mapping phases and crystal orientations with short acquisition times (10–20 ms/pixel) in a transmission electron microscope similarly to the Electron Backscattered Diffraction (EBSD) or Transmission Kikuchi Diffraction (TKD) techniques in a scanning electron microscope. In this study, we apply this technique to the characterization of deformation microstructures in an aggregate of bridgmanite and ferropericlase deformed at 27 GPa and 2,130 K. Such a sample is challenging for microstructural characterization for two reasons: (i) the bridgmanite is very unstable under electron irradiation, (ii) under high stress conditions, the dislocation density is so large that standard characterization by diffraction contrast are limited, or impossible. Here we show that detailed analysis of intracrystalline misorientations sheds some light on the deformation mechanisms of both phases. In bridgmanite, deformation is accommodated by localized, amorphous, shear deformation lamellae whereas ferropericlase undergoes large strains leading to grain elongation in response to intense dislocation activity with no evidence for recrystallization. Plastic strain in ferropericlase can be semiquantitatively assessed by following kernel average misorientation distributions.

Plain Language Summary We present a microstructural characterization of a mineralogical assemblage of the lower mantle deformed in the pressure-temperature conditions of the upper most lower mantle. We show that the magnesium silicate perovskite named bridgmanite is stiffer and deforms only along very localized shear bands. The magnesium oxide ferropericlase is much more ductile and takes most of the plastic strain.

1. Introduction

Deformation-induced microstructures carry critical information on the microscopic processes of deformation, hence on the relevance of deformation experiments for processes operating in the Earth's interior. Such characterizations are critical because the experimental conditions of deformation are vastly different from those in Earth's interior particularly in strain rate. For deformation under the shallow mantle conditions, experimental studies are straightforward (e.g., Karato et al., 1986; Mei & Kohlstedt, 2000), and a comparison of microstructures of experimentally deformed samples with those of naturally deformed rocks provides a guide to justify the extrapolation in strain rate (e.g., Karato & Wu, 1993).

The situation is very different for deformation in Earth's deep interior such as the lower mantle. Quantitative studies on deformation under the lower mantle pressure-temperature conditions and controlled strain rate became possible only recently (Girard et al., 2016). The experimental study by Girard et al. (2016) was conducted under the shallow lower mantle conditions (P = 27 GPa, T = 2,130 K) at a typical laboratory strain rate ($\sim 3 \times 10^{-5}$ s^{-1}). This provides the first opportunity to understand the processes of plastic deformation in the lower mantle. However, common to all experimental studies on plastic deformation, strain rates used are much higher (about 10 orders of magnitude, see, for instance, Paterson, 1987) than those expected in Earth, and stress needed to deform samples in these experiments (1–5 GPa) is substantially higher than those estimated for Earth's interior. Consequently, before applying these results, one needs to understand the microscopic processes of deformation.

Important microstructural observations include grains morphologies and the distribution of grain size, but also the intragranular defects contents: dislocations, their nature, and microstructures. Preliminary observations on grain morphology were reported by Girard et al. (2016) that provide evidence for stronger elongation of ferropericlase grains compared to bridgmanite. However, no characterization of defects microstructures has been performed to constrain active deformation mechanisms. Such a study is challenging because of technical difficulties including the high sensitivity of bridgmanite against electron beam radiation and the large strains involved in these experiments. Here we use a newly developed technique involving orientation and local misorientation mapping in transmission electron microscopy (TEM) to overcome these limitations.

Microstructures that develop as a result of plastic deformation are constituted of patterns of dislocation. Traditionally these features are studied by diffraction contrast in the TEM provided the dislocation density is not too high. For dislocations densities larger than ca. 10^{15} m^{-2}, individual dislocation contrasts overlap and cannot be resolved. Other parameters or proxies must then be found to follow the evolution of the plastic behavior. In 1993, Argon and Haasen (1993) have argued that a square root scaling law would describe the dependence of the mean, intragranular, misorientation angle θ_{mean} on plastic strain due to random fluctuations in the long-range strain field of dislocations:

$$\theta_{mean} \propto \sqrt{\varepsilon} \quad (1)$$

Some studies on microstructural evolution in deformed fcc metals and alloys have confirmed that plastic strain scales with misorientation (Hughes et al., 1997, 1998). Although, so far, these scaling laws have only been tested on metals, it is still interesting to note that they were found to be quite robust being independent of material properties such as stacking fault energy, solute content, etc., and process parameters such as temperature, strain, strain rate, strain paths, etc., suggesting a rather universal behavior. Intragranular misorientations can be detected in the reciprocal space through X-ray peak broadening which can be analyzed to provide average measurements of strain, including dislocation densities (Nyilas et al., 2006) and even information on Burgers vectors and slip systems (Cordier et al., 2004; Nisr et al., 2012). In the real space, scanning electron microscope (SEM)-based Electron Backscattered Electron Diffraction (EBSD) provides a very efficient and largely automated technique to sample long-range and short-range information on misorientations within deformed samples. Within the last decades, misorientations-based approaches have been used by metallurgists to follow the evolution of substructures during static and dynamic deformations (or loadings) (e.g., Schayes et al., 2016; Wright et al., 2011; Zhong et al., 2007).

In this paper, we present an alternative approach to SEM-based EBSD where orientation maps are obtained in the TEM from microbeam spot patterns. Compared to EBSD, this technique has several advantages. Being carried out in a TEM it benefits from the spatial resolution which results from the probe size, but also from the use of a thin foil. Also, TEM uses higher voltages which induce less damage in beam sensitive materials and spot patterns are less sensitive to the defect content and much more adapted to analyze highly deformed materials (see for instance, Figure 4 in Bollinger et al. (2015)). Of course, there are also some disadvantages, such as the need to prepare electron-transparent foils or the size of the sampled area which can be a strong limitation regarding the number of grains analyzed (especially if crystal preferred orientations were to be considered).

Here we apply scanning precession electron diffraction (SPED) to a high-pressure assemblage of bridgmanite and ferropericlase, shear deformed at large strains (of the order of 100%) in conditions of the uppermost lower mantle (Girard et al., 2016). Our goal is to study the defect distribution in bridgmanite and ferropericlase to better understand their deformation mechanisms at high-pressure and high-temperature. This is important to assess the scalability of the laboratory data to natural conditions.

Table 1
Samples Studied: Synthesis and Deformation Conditions

Run number	Pressure (GPa)	Temperature (K)	Strain (%)	Strain rate (s^{-1})
K1481	24	1,873	0	N.A.
Gamma 21 (G21)	27	2,130	100	5×10^{-5}

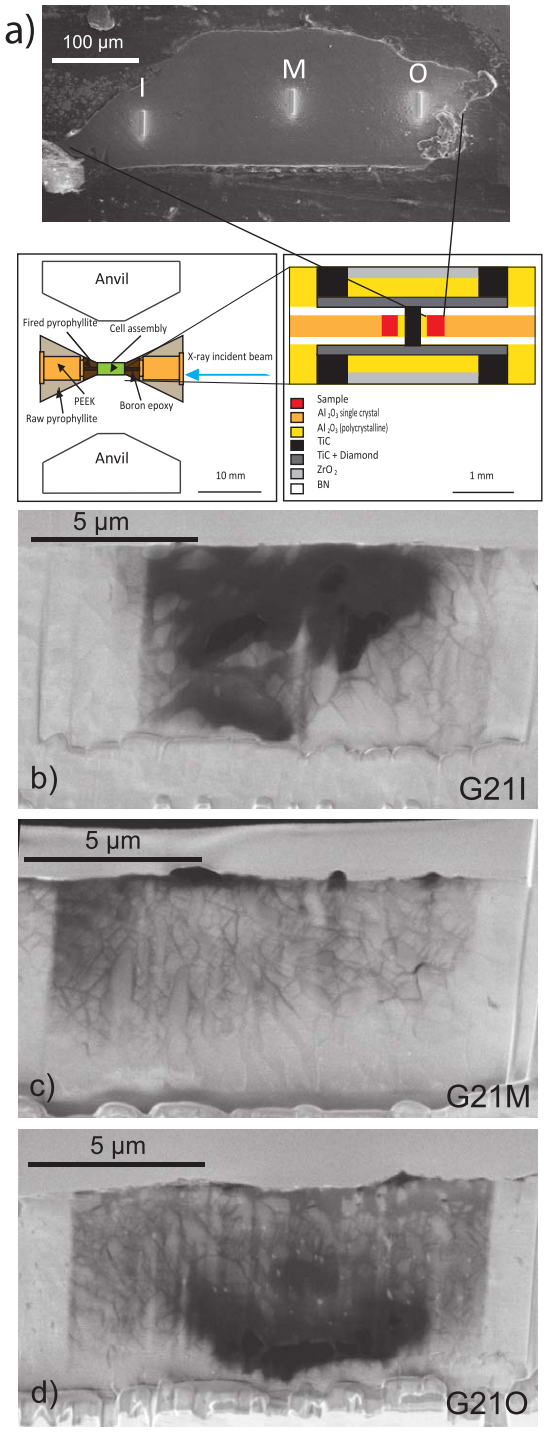

Figure 1. (a) Sketch of the deformation experimental setup with the locations where the three thin foils investigated in this study were extracted from Gamma 21. Their names are given according to their positions inner (I), middle (M), and outer (O): (b) FIB thin section G21I ("I" for inner position: lower strain), (c) FIB thin section G21M from the middle, and (d) FIB thin section G21O ("O" for outer position: higher strain).

2. Experimental Setup

2.1. Samples

Two samples have been investigated in this study. Their conditions of elaborations are summarized in Table 1.

The bridgmanite and ferropericlase assemblage have been synthesized under hydrostatic conditions during run K1481 using a Kawai type multi-anvil at Yale University (Table 1). The starting material, San Carlos olivine $(Mg_{0.9},Fe_{0.1})_2SiO_4$, was loaded in a molybdenum capsule, in an 8/3 cell assembly with a $LaCrO_3$ Furnace. The sample was annealed for 70 min at 24 GPa, 1,873 K. Pressure was estimated using pressure versus load calibration curve and temperature was estimated from power versus temperature calibration curve. The sample was then cut into 200 μm thick discs, and then cut into half ring (ID = 0.45 mm, OD = 1 mm) to be used in the Rotational Drickamer Apparatus (RDA) for deformation experiment (run Gamma 21).

Run Gamma 21 (Table 1) was performed using the RDA at the NSLS synchrotron beamline X17B2. A cross section of the cell assembly used at the beamline is shown in Figure 1. The sample was first compressed, then annealed for 60 min before starting the deformation. Pressure and temperature were estimated by in situ X-ray diffraction data obtained during annealing, using bridgmanite and ferropericlase equation of state (Komabayashi et al., 2010; MaO et al., 1991; Tange et al., 2012). Because the X-ray synchrotron beam has been lost at the beginning of the deformation, total strain was estimated from the angle of rotation of the anvil and the relationship between the angle of rotation and shear strain based on the previous results.

Electron-transparent foils (Figures 1b–1d) for TEM were extracted from the as-transformed (K1481) and HP-deformed (Gamma 21) samples using the focus ion beam technique with a FIB Dual Beam FEI Strata DB 235.

2.2. Transmission Electron Microscopy

TEM investigations were performed with a FEI® Tecnaï $G^2$20Twin microscope, operating at 200 kV and with a FEI CM30 microscope operating at 300 kV, both with a LaB_6 filament and using a double tilt sample-holder.

Orientation maps were acquired with a step size of 5 nm using SPED in the TEM with the ASTAR™ tool from NanoMEGAS (Rauch & Véron, 2014). The TEM is set in microbeam mode (spot size 4 nm) and the incident electron beam is scanned over the area thanks to a dedicated hardware control system of the TEM deflecting coils. The individual exposure time at each location is 10 or 20 ms. The spot patterns are collected with an external Stingray CCD camera that points on the TEM phosphorous screen and stored in the computer memory for further indexation and postprocessing. The diffraction patterns were collected as 144 × 144 pixels at a camera length of 89 mm. Electron diffraction spot patterns are indexed (providing the local crystal orientations) by comparing individually obtained patterns via cross-correlation matching techniques with precalculated electron diffraction templates generated every 1° (orientation resolution). For bridgmanite, templates have been generated from the crystallographic data of Tschauner et al. (2014). All crystallographic data for bridgmanite are presented within the *Pbnm* space

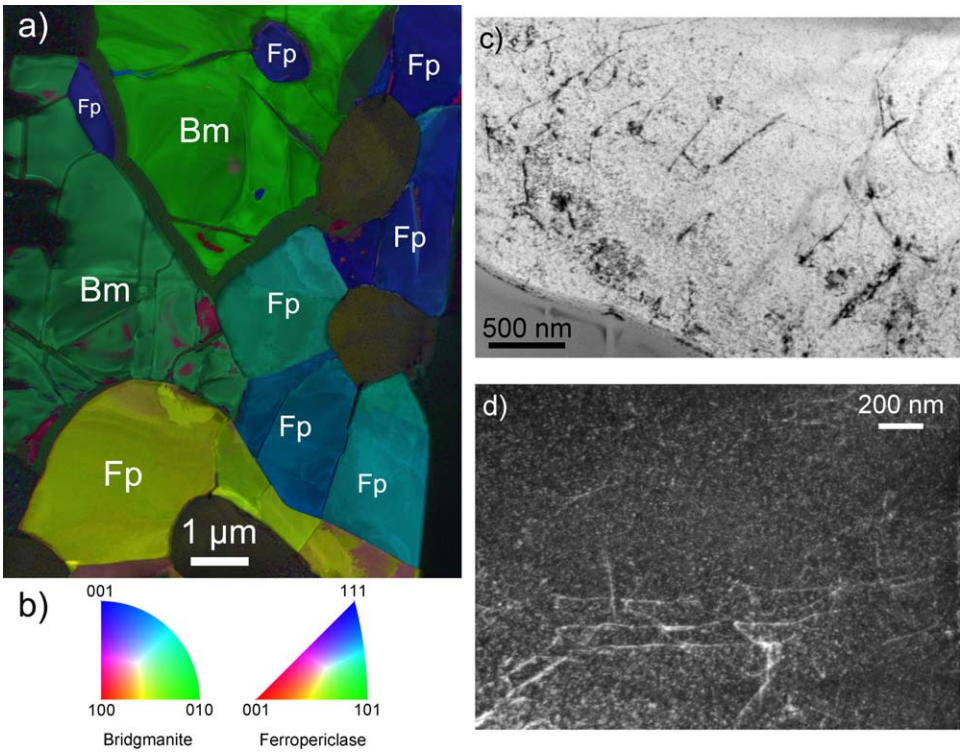

Figure 2. Starting material K1481. (a) Orientation map-spatial resolution 5 nm-1,600 × 2,000 data points—inverse pole figure (IPF). For each phase, the color indicates the crystallographic orientation of the vertical direction. Bm stands for bridgmanite and Fp for ferropericlase. (b) Color code for the crystallographic orientations of the IPF in Figure 2a. Ferropericlase is indexed within the *Fm3m* space group and bridgmanite within the *Pbnm* space group. (c) Ferropericlase: TEM bright field showing dislocations (dark lines) with a density of the order of 10^{12}–10^{13} m^{-2}. The spotty aspect in the background is due to damage induced by ion bombardment. (d) Ferropericlase: TEM dark field showing dislocations (white lines) with a density of the order of 10^{12}–10^{13} m^{-2}.

group (where a = 4.82 Å, b = 5.05 Å, and c = 6.92 Å). Ferropericlase templates were calculated from crystallographic data from Fei et al. (1992).

In this study, we used precession illumination in the TEM. When the precession mode is activated, a hollow-cone illumination is formed with the upper coils and equal and opposite signal is applied to the lower coils to bring the tilted beam back onto the optic axis. The net effect of the double-rocking is equivalent to having a stationary beam and a crystal which would precessed about the optic axis. The great advantage of this technique is that many more reflections are seen in the diffraction pattern and the intensity distribution gets closer to the kinematical diffracting conditions. We used precession angles in the range 0.5–1°. The orientations maps are presented as inverse pole-figures (IPF), where the color at each position represents the crystal orientation, that is, for the shear deformed sample, parallel either to the shear direction (SD), the radial direction (RD), or the compression direction (CD, i.e., parallel to the axis of the anvils). No cleaning procedure was applied to these maps. From the orientation maps, virtual bright field (VBF) maps can be generated which represents the fluctuation of the central beam intensity of the diffraction patterns. This builds up a STEM-like bright field contrast directly related to the orientation maps. The quality of indexation from template matching is quantified by the image correlation index, $Q(i)$, which is calculated for every template (Rauch & Dupuy, 2005):

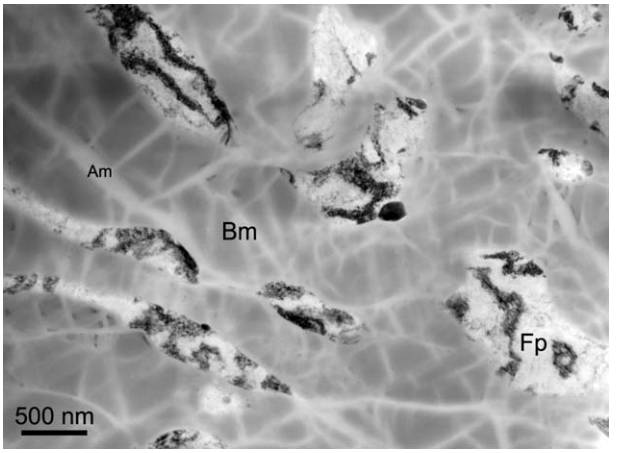

Figure 3. Overall microstructure of G21M (middle position). TEM bright field. Bm stands for bridgmanite, Fp for ferropericlase, and Am for amorphous material. In this sample, bridgmanite is well preserved although the grains contain pervasive amorphous lamellae.

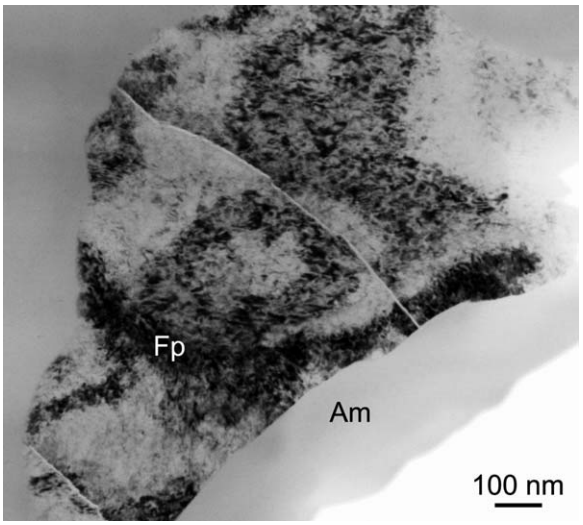

Figure 4. G21I (inner position). TEM bright field. Fp, ferropericlase and Am, amorphous material. All ferropericlase grains contain a very large density of dislocations, which precludes visualizing individual defects.

$$Q(i)=\frac{\sum_{j=1}^{m} P(x_j,y_j)T_i(x_j,y_j)}{\sqrt{\sum_{j=1}^{m} P^2(x_j,y_j)}\sqrt{\sum_{j=1}^{m} T_i^2(x_j,y_j)}} \quad (2)$$

In this expression, the diffraction pattern is represented by the intensity function $P(x,y)$ at each position (x,y) and each template i is described by the function $T_i(x,y)$. The highest Q value corresponds to the solution. The reliability of this solution can be quantified by the ratio of the matching indices for the two best solutions Q_1 and Q_2:

$$R=100\left(1-\frac{Q_1}{Q_2}\right) \quad (3)$$

In reliability maps, the brighter the pixel (i.e., the highest the reliability index) the more reliable is the indexation proposed. On the contrary, the darker is the pixel, the least reliable is the solution. This is typically the case at grain boundaries where two solutions of coexisting grains overlap or when for some reasons, the quality of the diffraction patterns is less. The presence of amorphous material represents an extreme case of that situation.

SPED can be compared with EBSD performed in transmission in an SEM (originally called t-EBSD for transmission EBSD or TKD for transmission Kikuchi diffraction). Both use electron-transparent thin foils and work in transmission. TKD is based on low-energy transmission Kikuchi diffraction in an SEM (Keller & Geiss, 2012; Suzuki, 2013; Trimby, 2012) whereas SPED involves high-energy microdiffraction in the TEM. It is important to highlight that the ASTAR™ algorithm saves all diffraction patterns and that no original data are lost. This is a huge advantage compared to commercial (standard) EBSD techniques which are usually not saving patterns and never perform image matching. Instead, in standard EBSD, indexing is based on Hough-transforms of the pattern for indexing and in most scenarios only the indexing is saved and the original data, namely the Kikuchi patterns, are discarded. From that perspective, SPED performed with ASTAR can be compared to the Dictionary Indexing approach for EBSD indexing, which also saves all patterns and performs image matching for indexing against a library of precomputed patterns (Marquardt et al., 2017; Ram et al., 2017; Singh & De Graef, 2016, 2017). If reliable results in terms of angular resolution (HR-EBSD or HR-KAM, cf. Britton et al., 2010) are needed, high-resolution patterns must be acquired (1,600 × 1,000 pixels). This results in an extremely large set of data to postprocess. In the most common TKD setups (except for Brucker), the EBSD camera is not in the most suitable condition for pattern acquisition and the patterns are generally deformed. This could

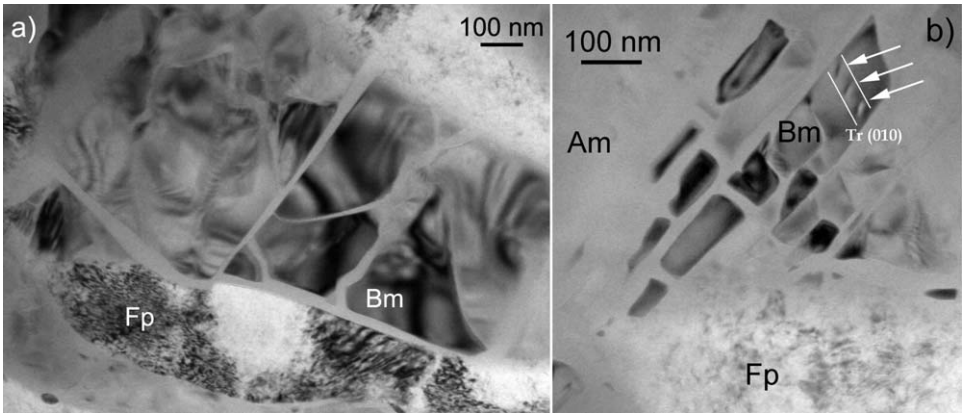

Figure 5. G21M (middle position). TEM bright field (Bm, bridgmanite; Fp, ferropericlase; and Am, amorphous material). The remaining crystalline bridgmanite parts are set in Bragg orientation to promote diffraction contrast. No evidence for defects is found in any grains besides the three dislocations arrowed in Figure 5b. See text for the analysis of the trace of the glide plane.

result in lower angular resolution that conventional EBSD. Still, TKD looks superior to SPED in term of angular resolution, but this advantage disappears with beam sensitive samples. The acquisition rate should be much higher with TKD to avoid beam damage and requires new technology which only becomes available.

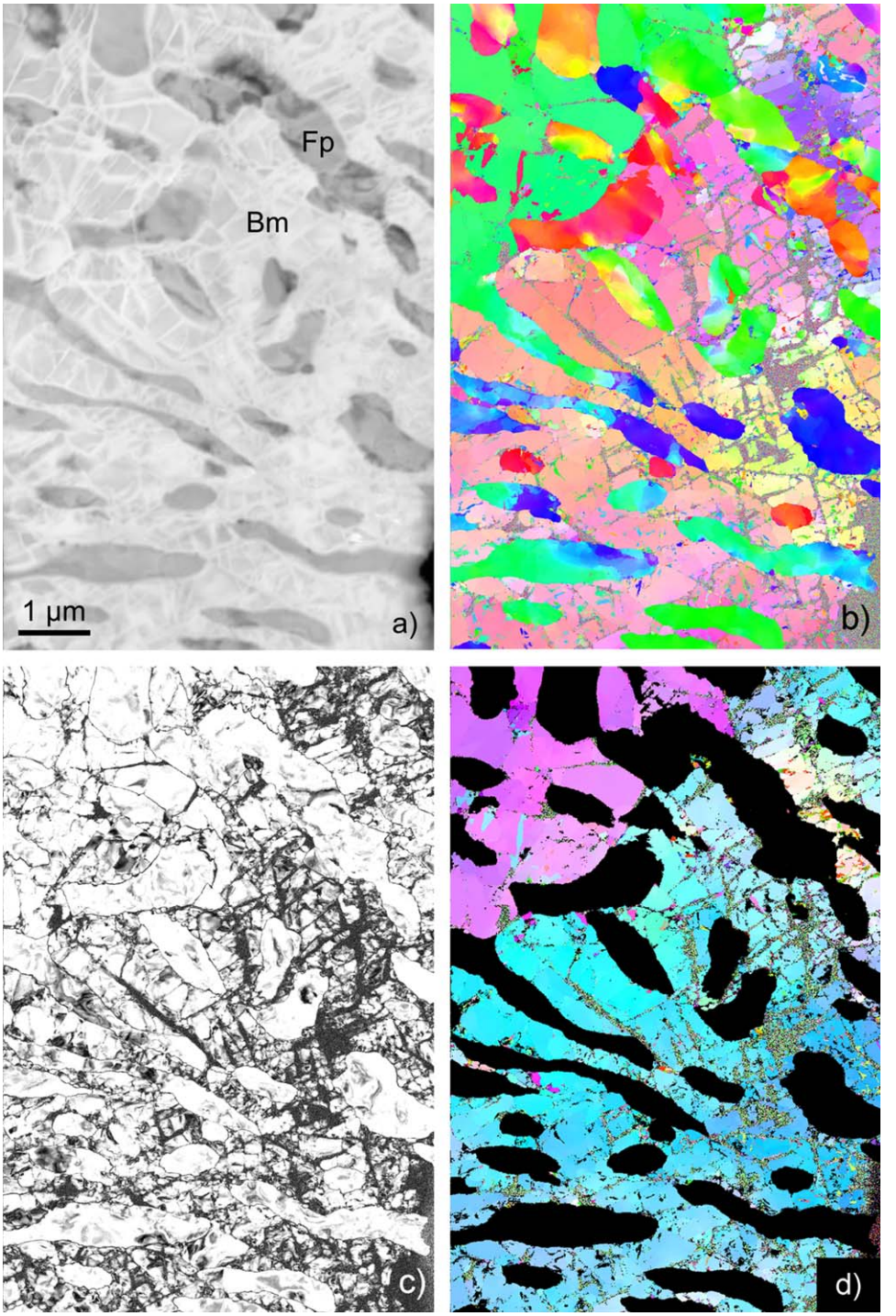

Figure 6. G21M (middle position). (a) SPED-virtual bright field. Spatial resolution 5 nm-1,200 × 1,800 data points. (b) SD-IPF: inverse pole figure map corresponding to the shear direction (horizontal). (c) Reliability map (plotted between 0 and 35). Less reliable places appear dark. (d) RD-IPF: inverse pole figure map of bridgmanite corresponding to the radial direction (perpendicular to the map plane). (e) CD-IPF: inverse pole figure map of ferropericlase corresponding to the compression direction (vertical). (f) IPF color legend. Ferropericlase is indexed within the *Fm3m* space group and bridgmanite within the *Pbnm* space group.

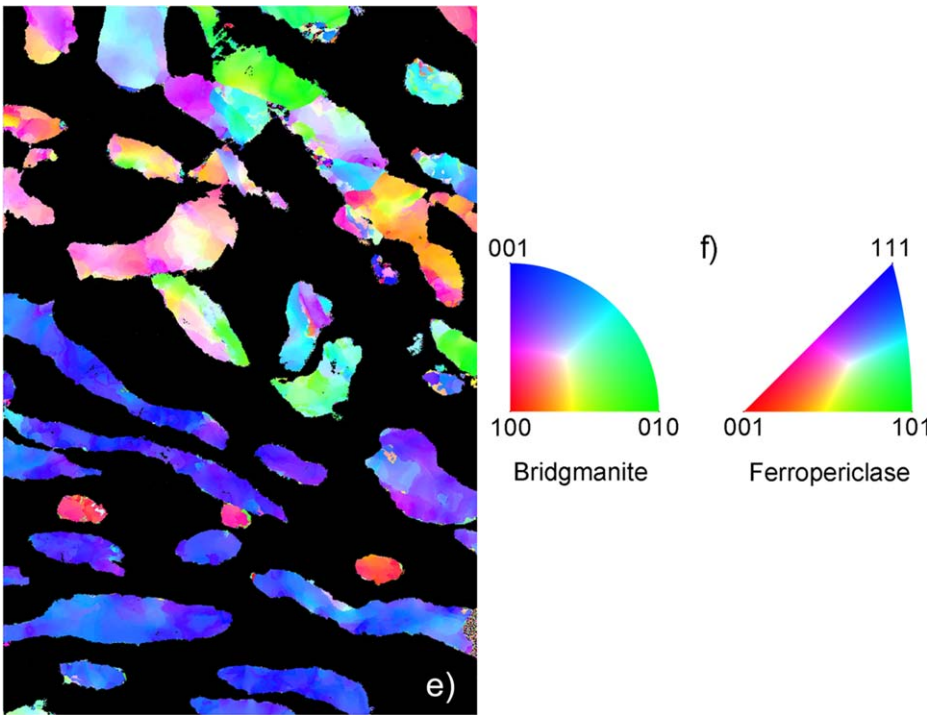

Figure 6. (Continued).

Although Q-maps have been proposed as a first approach to detect residual plastic strain, several parameters can affect this parameter as discussed above (Wright et al., 2011). In this study, we rather focus on the measurements of local misorientations as recently developed in the EBSD community (e.g., Wright et al., 2011). Postprocessing of the orientation maps was performed with the TSL OIM^{TM} Analysis 7 commercial software provided by EDAX. As commonly used in EBSD, several quantities are calculated from the orientation maps:

1. The *Kernel Average Misorientation* (KAM) calculates the average misorientation between a pixel and its neighbors provided that the misorientation does not exceed a predefined threshold value, e.g., 5°, thus the incorporation of well-defined grain boundaries is avoided. If plastic deformation results from dislocation glide and crystal lattice rotation, this approach allows quantitative evaluation of the local plastic strain gradients (Godfrey et al., 2005). A kernel is a set of points of prescribed size surrounding the scan point of interest. The size of the kernel is generally prescribed to the *n*th nearest-neighbors. Hence, this parameter is sensitive to the step size of the measurement grid.
2. The *Grain Orientation Spread* (GOS) is the average deviation in orientation between each point in a grain and the average orientation of the grain. This approach leads to assigning the same value of the GOS to every scan point contained within a grain.
3. The *Grain Reference Orientation Deviation* (GROD) is based on the misorientation between a reference point of that grain and the other points. The reference point can be the mean misorientation of the grain (in that case the GROD is also called *Mis2mean* in MTEX) or the point of the grain where the KAM is the lowest.

KAM, GROD, and GOS approaches appear to be complementary. GROD maps show the orientation field referenced to a fixed point whereas KAM approach shows the magnitude of the gradient, which can be seen as the first derivative of the orientation field.

3. Observations

3.1. Starting Material (K1481)

The microstructure of the starting material is illustrated in Figure 2. As already reported in Girard et al. (2016), it consists in a mixture of bridgmanite and ferropericlase grains which are mostly equiaxed. With

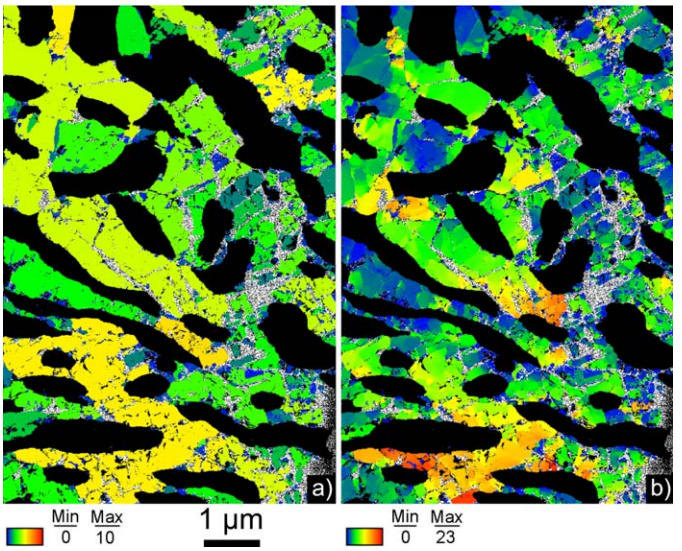

Figure 7. Bridgmanite in G21M (middle position). Same map area as Figure 6. (a) Grain Orientation Spread (GOS) map. Each grain displays a color corresponding to its average internal misorientation. (b) Grain Reference Orientation Deviation (GROD) or Mis2mean map since here, the reference is the mean misorientation in each grain. This representation highlights intragranular misorientations which would correspond to small color changes in Figures 6b, 6d, and 6e.

conventional bright-field TEM analyses, only ferropericlase shows some dislocations, with a density of the order of 10^{12}–10^{13} m^{-2} at the most (Figures 2c and 2d).

3.2. Conventional TEM Observation of Gamma 21

Although ferropericlase is found equally well in the three thin foils, the preservation of bridgmanite after FIB milling is very uneven. In G21M, crystalline bridgmanite has been well preserved everywhere in the thin section although this phase contains systematically numerous amorphous lamellae (Figure 3). In G21I, most bridgmanite has been amorphized in the central part of the thin section. Almost no bridgmanite is preserved in G21O.

The strong plastic strain of ferropericlase is suggested by the elongated shape of most grains (already observed at the SEM: Girard et al., 2016) as seen in Figure 3 (with clearer evidence in Figure 6e) in G21M, but also from the very large dislocation density which prevents further analysis with conventional techniques (Figure 4).

In bridgmanite, rapid amorphization under the electron beam prevents from having an exhaustive characterization of the microstructure. However, the only remaining crystalline areas are remarkably free of dislocations (Figure 5a). Only three dislocations have been observed, they are displayed in Figure 5b. Taking into account the orientation of the grain (close to the zone axis [746]) from the orientation map (see below), the orientation of the trace of the glide plane, and the thickness of the thin foil, one finds that the plane containing the dislocations is compatible with (010). One notes the pervasive occurrence of amorphous lamellae which preexisted observation (but broaden rapidly under the beam). It is worth mentioning that, because of the sensitivity of the samples to the beam, we took care to record the orientation maps described below before any exposure of the samples and that the conventional TEM investigation has been done only at the end of the study.

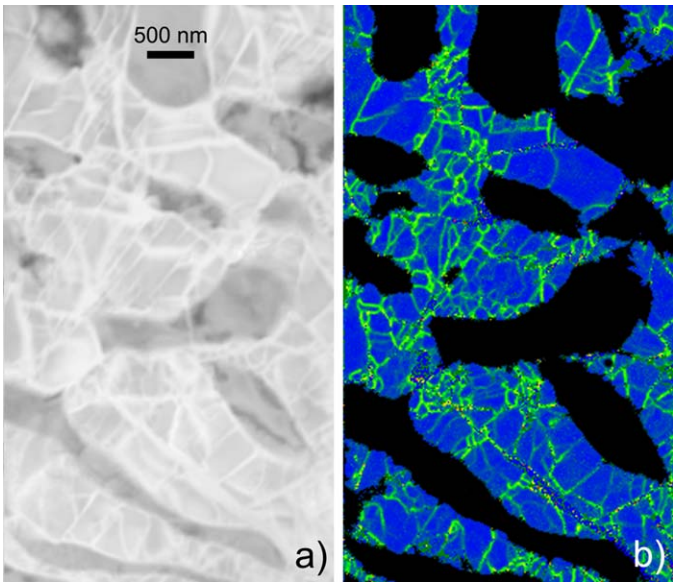

Figure 8. Origin of amorphous lamellae in bridgmanite from G21M (middle position). (a) SPED-virtual bright field where the amorphous lamellae in bridgmanite appear brighter than the crystalline parts (ferropericlase appear even darker). (b) Kernel Average Misorientation (KAM—third neighbor) in bridgmanite. This representation highlights local gradients of orientation. One can see that amorphous lamellae correlate with high KAM, demonstrating that they localize shear and thus have a mechanical origin and do not result from sample preparation.

3.3. Orientation Imaging Mapping on Gamma 21

To gain more information on the deformation, we have acquired orientation maps by SPED with the ASTAR™ system. Figure 6 shows the maps obtained on G21M (which is the sample for which both phases are best preserved). The virtual bright field shows the microstructure of the two phases, and also the amorphous lamellae later imaged in TEM bright field. From the indexation of the diffraction patterns, it is possible to plot the IPF maps either corresponding to the shear direction, to the compression direction or to the radial direction. In Figure 6b, we present the IPF of both phases corresponding to the shear direction (SD). It is possible to separate both phases as shown in Figures 6d and 6e. The indexation is usually very good. This can be assessed from the reliability map (Figure 6c). The reliability drops at the grain boundaries when the diffraction patterns consist in the superposition of those of the two grains. The reliability map thus offers a good visualization of the grain boundaries. The reliability is also poor in thicker areas or when crystallinity is less. Such is the case in some places in bridgmanite, for instance along the thickest amorphous lamellae (Figures 6c and 6d).

3.3.1. Bridgmanite

The orientation map of bridgmanite from Gamma 21 reveals rather large grains (several micrometers) which contain elongated ferropericlase grains. The colors are not perfectly uniform in the IPF suggesting

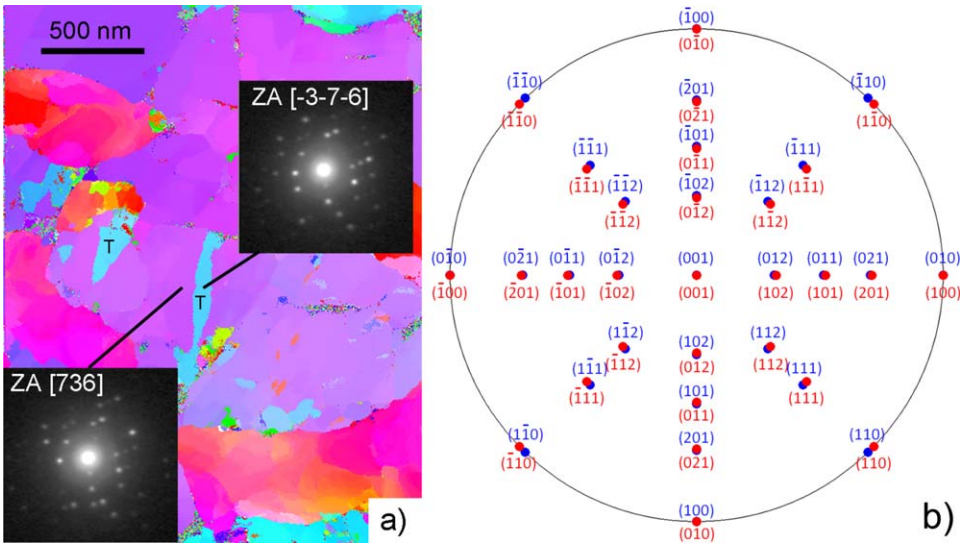

Figure 9. G21M (middle position). (a) CD-IPF (enlargement) showing twinned domains *T* (see text) with corresponding diffraction patterns (indices are given within the *Pbnm* space group). (b) Twin model resulting from the switch of the [100] and [010] axis (*Pbnm* space group) corresponding to an 87.3° rotation around [001].

some misorientation in the bridgmanite grains. The GOS (Figure 7a) is well suited to reveal these variations and quantify them. It shows that all bridgmanite grains (or domains within those grains) exhibit significant internal misorientation. The GROD (Figure 7b) shows that these misorientations are pervasive and rather heterogeneous. The GROD seems to be more pronounced when bridgmanite forms narrow channels between elongated ferropericlase grains suggesting strain resulting from the infiltration process of ferropericlase grains.

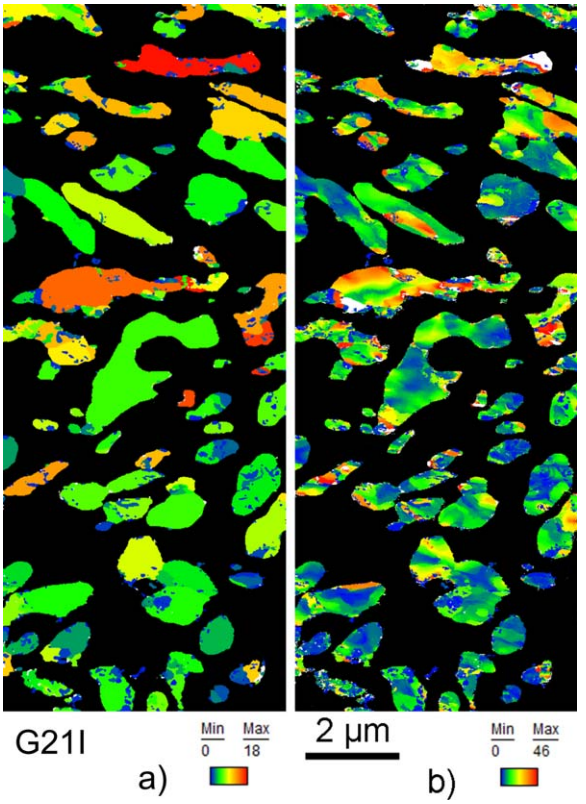

Figure 10. Ferropericlase in G21I (inner position see Figure 1). Total map acquired with a spatial resolution 5 nm-1,200 × 3,000 data points. (a) Grain Orientation Spread (GOS) and (b) Grain Reference Orientation Deviation (GROD) using the average orientation for each grain as the reference (Mis2mean).

Further understanding comes from plotting point to point misorientation profiles across the amorphous lamellae. This shows that these lamellae correspond to jumps of misorientation between largely undeformed regions (supporting information Figure S1). These features appear well on the KAM maps, which highlight places where strong misorientation localizes. Comparison of the KAM with the TEM bright field or the SPED-virtual bright field (Figure 8) demonstrates that misorientation gradients correlate very well with the amorphous lamellae. These lamellae thus appear to be the location where deformation localized in bridgmanite.

In bridgmanite, some domains attract attention (Figure 9a or Figures 6b and 6d (upper left corner)). They exhibit a remarkable misorientation with the surrounding matrix of $87.4 \pm 0.1°$. The analysis of the diffraction patterns of both domains shows that they correspond to switching the [100] and [010] axis, i.e., to the {110} pseudomerohedral twinning of the *Pbnm* orthorhombic structure already reported (e.g., Wang et al., 1992). Indeed, this model (Figure 9b) predicts a theoretical misorientation of 87.3° between the variants which is in excellent agreement with the value found experimentally.

3.3.2. Ferropericlase

As already mentioned above and in Girard et al. (2016), the morphology of the ferropericlase grains is already a strong indication of large strain in this phase. It seems that from the inner to the outer sample there is a gradient in the microstructure with more elongated (G21M) and then fragmented (G21O) ferropericlase grains as one goes

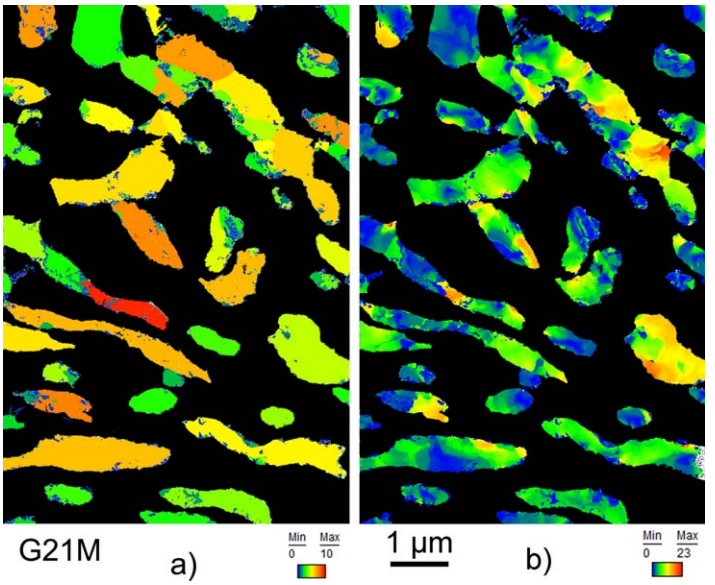

Figure 11. Ferropericlase in G21M (middle position). Same map area as Figure 6. Total map acquired with a spatial resolution 5 nm-1,200 × 1,800 data points. (a) Grain Orientation Spread (GOS) and (b) Grain Reference Orientation Deviation (GROD) using the average orientation for each grain as the reference (Mis2mean).

from inside to outside the deformation sample. The GOS maps (Figures 10a, 11a, and 12a) show that all grains are strongly internally disoriented (i.e., deformed). Comparison is, however, quite difficult since heterogeneities lead to use different scales. The GROD maps (Figures 10b, 11b, and 12b) show that the indistinct, large dislocation densities observed in the TEM bright-fields hide some complex, heterogeneous structures at a very fine scale. One can understand that such strong local heterogeneities can ultimately lead to fractures during foil thinning as seen in Figure 4.

4. Discussion

TEM-based SPED appears as a powerful complement to in situ X-ray diffraction to study the plastic behavior of high-pressure phases, especially in case of samples that include beam sensitive minerals and also aggregates of phases exhibiting a large viscosity contrast. In the present case, in situ X-ray diffraction acquired during deformation provided information on stress against shear strain. Where strain, obtained from a marker or (here) from the rotation of the anvils, could only be assessed on average, in situ X-ray diffraction provides information which can distinguish both phases. Using this technique, Girard et al. (2016) could demonstrate that ferropericlase is much softer than bridgmanite at 27 GPa and 2,130 K, with average flow stress 4–5 times smaller in ferropericlase than in bridgmanite. SEM, backscattering images of the recovered Gamma 21 already showed (Girard et al., 2016) that ferropericlase grains undergone strains much larger than the average value of the sample estimated to 100%.

Our microscopic investigation confirms these observations. Prior to deformation, ferropericlase in K1481 is often larger than 1 μm and rather equiaxed (Figure 2). After deformation (Figures 6 and 10−12), the grains of ferropericlase are strongly stretched, eventually leading to fragmentation into grains of a few hundreds of nanometers in size. These processes have been observed in monomineralic magnesiowüstite deformed in shear for ca. $\gamma = 5$ to ca. $\gamma = 10$ (Heidelbach et al., 2003; see also similar observations in halite deformed under large shear strains: Wenk et al., 2009). We can see in Figure 6e that most grains in the lower part of the map exhibit very close orientations. We can speculate that they result from the stretching and fragmentation of a single larger grain of ferropericlase. It is difficult from a cross section only to decide whether this also corresponds to a three-dimensional interconnectivity in G21M. Conventional TEM observations show further evidence of accumulated strain with very large dislocations densities. In the starting material, the dislocation density was found to be of the order of 10^{12}–10^{13} m^{-2}. In ferropericlase from Gamma 21, the dislocation densities are much larger. They are so large that no measurement of dislocation density is now possible. This illustrates the usual limitation of TEM studies on samples deformed at large strains. Here we show how SPED can overcome this limitation.

Beyond the shape of the grains and without directly imaging the dislocations, the IPF of ferropericlase (Figure 6e) show that grains do not exhibit a single orientation. Indeed misorientation profiles show extremely strong gradients inside every grains. To gain more information on these misorientations, we have applied the standard posttreatments used in EBSD. First, we used the grain-based method to better reveal the presence of intracrystalline misorientations. The GOS affects a single value (taken as the average) for the misorientation to a body identified as a grain.

Figures 10a, 11a, and 12a show that all ferropericlase grains, even the smallest, exhibit average misorientations of several degrees. The spatial distribution of those misorientations is better illustrated using the GROD, which represents at each measurement point the misorientation with a reference value. Here we choose the average misorientation as the reference. The GROD is then usually called the Mis2mean. The Mis2mean maps (Figures 10b, 11b, and 12b) show that deformation in ferropericlase is very heterogeneous at a very small scale. This information could not be withdrawn from standard diffraction contrast imaging (e.g., Figure 4). Being cubic, ferropericlase exhibits a large number of equivalent slip systems which involve dislocations which can interact

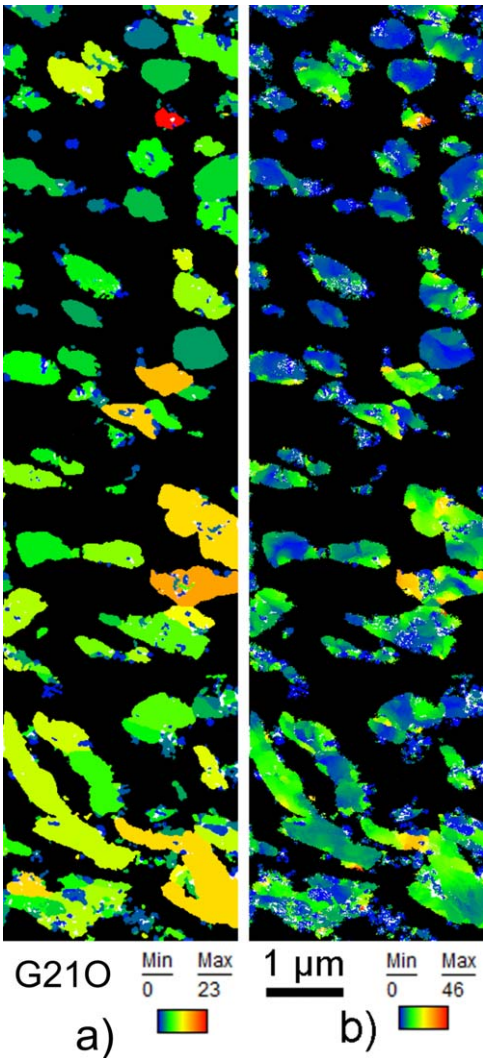

Figure 12. Ferropericlase in G21O (outer position). Total map acquired with a spatial resolution 5 nm-600 × 2,400 data points. (a) Grain Orientation Spread (GOS) and (b) Grain Reference Orientation Deviation (GROD) using the average orientation for each grain as the reference (Mis2mean).

and form various kinds of junctions. This is the origin of strong dislocation storage in this material which can lead to significant strain hardening (Amodeo et al., 2014). Usually, this dislocation storage leads to recrystallization, i.e., to the formation of new grains free of dislocations, even in single crystals (see, for instance, Mariani et al., 2009). Here we find no evidence of dislocation-free grains or domains. Further quantification is difficult. Indeed, the grain grouping algorithms (GOS and GROD) are by definition sensitive to the body considered as a grain. A usual criterion is to consider a limit of misorientation of 15° as a standard limit to discriminate subgrains and grain boundaries. In the present case, ferropericlase grains are strongly deformed and present strong misorientations which challenge the automatic detection of "grains." Hence, we consider that GOS and GROD are useful to highlight the strong strains undergone by the ferropericlase grains, but not well adapted to further quantification. We prefer here to rely on short-range misorientation parameters with a kernel-based algorithm like the KAM. In that case, to provide comparable results, one must compare maps acquired with the same spatial resolution, and the same kernel size must be used. Figure 13 corresponds to maps acquired with a step size of 5 nm and processed with third nearest-neighbor kernels. Figure 13b shows in the case of ferropericlase that KAM distributions can resolve more quantitative information. The KAM distribution in K1481 is clearly distinct from those in Gamma 21. Being much narrower, indicating much less intragranular misorientation, it is clearly consistent with what is expected from the undeformed state. More interestingly, one also observes a consistent evolution of the KAM distribution with the sample position in the experimental setup. From the inner position to the outer position in the sample ring, one finds that (i) the KAM distribution peak shifts to higher values of misorientation, (ii) the peak fractions decrease, and (iii) the distributions broaden. This evolution is characteristic of increasing strain. One can see here that our analysis is able to evidence the radial strain gradient which is expected in a torsion test.

Although preservation of bridgmanite remains a challenging issue, we have been able to gather enough diffraction patterns on this phase to gain information on its deformation mechanisms. From G21M (which is the sample where bridgmanite is best preserved), one can essentially see two large grains with a morphology which cannot be distinguished from those in K1481. The GOS and GROD maps of those grains (Figure 7) show evidence of intragranular misorientation which suggests some deformation. The KAM distributions (Figure 13a) also show that Gamma 21 is clearly distinct from the undeformed state. The difference in the distributions from G21I and G21M is also consistent with a radial strain gradient although it is less conclusive than in ferropericlase. Here we get more information from the KAM map. In Figure 8, one can see an excellent correlation between the KAM spatial distribution and the presence of amorphous lamellae observed in the virtual bright field or in the TEM bright-field images. We interpret that these amorphous lamellae are regions where strain was localized during HP-HT deformation. The only information that we have to further constrain deformation mechanisms that were active at HP-HT comes from the three dislocations observed. Their alignment allows to infer their glide plane which is compatible with (010). Considering the possible slip systems predicted in bridgmanite (Ferré et al., 2007; Hirel et al., 2014; Mainprice et al., 2008), this suggests that the observed dislocation would belong to the [100](010) slip system. Our (single) observation is not compatible with the [001](100) slip system inferred by Tsujino et al. (2016) from crystal preferred orientation developments. We have also observed a few pseudomerohedral twins in bridgmanite. Twinning occurs and can be observed, but it is not pervasive, showing that twinning does not represent a significant deformation mechanism for bridgmanite under those conditions.

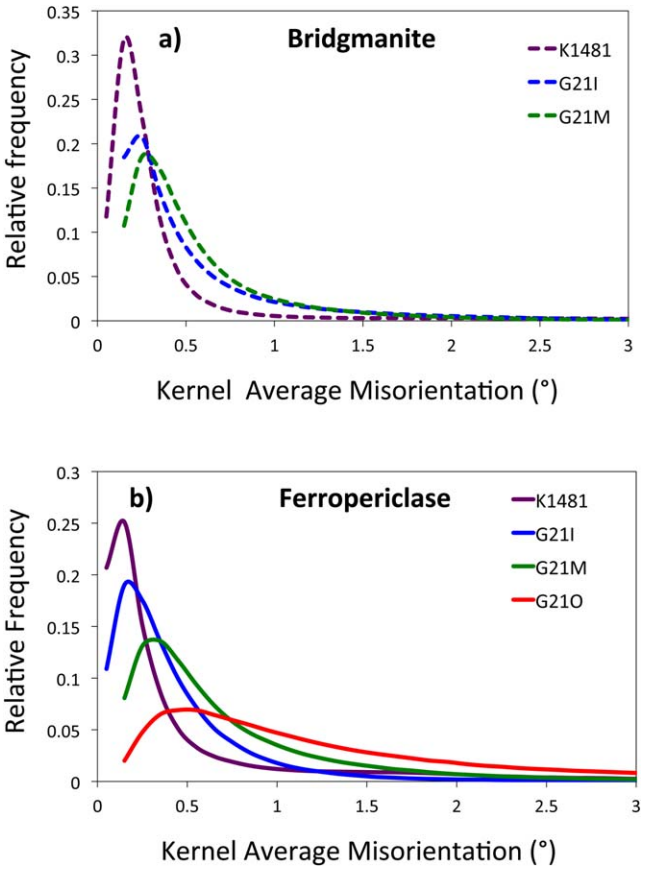

Figure 13. KAM distributions in undeformed and deformed bridgmanite and ferropericlase in each sample investigated here, i.e., for the deformed samples for increasing strains from the inner to the outer positions (see Figure 1). (a) Third nearest-neighbor KAM distributions in bridgmanite, where the starting material is compared with G21I and G21M. Since bridgmanite was completely amorphized in G21O, this sample is not represented here. (b) Third nearest-neighbor KAM distributions in ferropericlase for all samples including the starting material.

5. Conclusions

SPED represents a powerful new technique to analyze samples deformed at HP-HT. Applied to aggregates of bridgmanite and ferropericlase deformed in conditions of the uppermost lower mantle, it provides new information about the plastic behavior of those phases. We see only evidence form intracrystalline plasticity by dislocation motion although the deformed microstructure of bridgmanite and ferropericlase suggest very different mechanisms and plastic behavior. Ferropericlase shows strong evidence for large strains (much larger than the average 100% strain of the aggregate) with intense dislocation activity and storage leading to what we interpret as elongation leading to fragmentation of the grains. Despite these high strains, we observe no evidence for dynamic recrystallization. Evidence of deformation is demonstrated in bridgmanite although clearly less pronounced. It occurs essentially through localized, amorphous, shear deformation lamellae. An evidence for dislocations belonging to the [100](010) slip system is reported.

Acknowledgments
The work in Lille was supported by funding from the European Research Council under the Seventh Framework Programme (FP7), ERC grant 290424—RheoMan to P. Cordier. The TEM facility in Lille (France) is supported by the Conseil Regional du Nord-Pas de Calais, and the European Regional Development Fund (ERDF). We thank D. Troadec (IEMN-Lille) for sample preparation with the FIB. We are grateful to Dr. K. Marquardt and an anonymous reviewer for their comments which helped improving the manuscript. Data are available from https://figshare.com/s/4a19bbda734beef58be1.

References

Amodeo, J., Devincre, B., Carrez, P., & Cordier, P. (2014). Dislocation reactions, plastic anisotropy and forest strengthening in MgO at high temperature. *Mechanics of Materials*, *71*, 62–73.

Argon, A. S., & Haasen, P. (1993). A new mechanism of work hardening in the late stages of large strain plastic flow in F.C.C. and diamond cubic crystals. *Acta Metallurgica et Materialia*, *41*(11), 3289–3306. https://doi.org/10.1016/0956-7151(93)90058-Z

Bollinger, C., Merkel, S., Cordier, P., & Raterron, P. (2015). Deformation of forsterite polycrystals at mantle pressure: Comparison with Fe-bearing olivine and the effect of iron on its plasticity. *Physics of the Earth and Planetary Interiors*, *240*, 95–104. https://doi.org/10.1016/j.pepi.2014.12.002

Britton, T. B., Maurice, C., Fortunier, R., Driver, J. H., Day, A. P., Meaden, G., et al. (2010). Factors affecting the accuracy of high resolution electron backscatter diffraction when using simulated patterns. *Ultramicroscopy*, *110*(12), 1443–1453.

Cordier, P., Ungár, T., Zsoldos, L., & Tichy, G. (2004). Dislocation creep in $MgSiO_3$ perovskite at conditions of the Earth's uppermost lower mantle. *Nature*, *428*(6985), 837–840.
Fei, Y., Mao, H.-K., Shu, J., & Hu, J. (1992). P-V-T equation of state of magnesiowüstite $(Mg_{0.6}Fe_{0.4})O$. *Physics and Chemistry of Minerals*, *18*(7), 416–422.
Ferré, D., Carrez, P., & Cordier, P. (2007). First-principles determination of dislocations properties of $MgSiO_3$ perovskite at 30 GPa based on the Peierls-Nabarro model. *Physics of the Earth and Planetary Interiors*, *163*, 283–291.
Girard, J., Amulele, G., Farla, R., Mohiuddin, A., & Karato, S.-I. (2016). Shear deformation of bridgmanite and magnesiowüstite aggregates at lower mantle conditions. *Science*, *351*(6269), 144–147. https://doi.org/10.1126/science.aad3113
Godfrey, A., Cao, W. Q., Liu, Q., & Hansen, N. (2005). Stored energy, microstructure, and flow stress of deformed metals. *Metallurgical and Materials Transactions A*, *36*, 2371–2378.
Heidelbach, F., Stretton, I., Langenhorst, F., & Mackwell, S. (2003). Fabric evolution during high shear strain deformation of magnesiowüstite $(Mg_{0.8}Fe_{0.2}O)$. *Journal of Geophysical Research: Solid Earth*, *108*(B3), 2154. https://doi.org/10.1029/2001JB001632
Hirel, P., Kraych, A., Carrez, P., & Cordier, P. (2014). Atomic core structure and mobility of [100](010) and [010](100) dislocations in $MgSiO_3$ perovskite. *Acta Materialia*, *79*, 117–125.
Hughes, D. A., Chrzan, D. C., Liu, Q., & Hansen, N. (1998). Scaling of misorientation distributions. *Physical Review Letters*, *81*(21), 4664–4667.
Hughes, D. A., Liu, Q., Chrzan, D. C., & Hansen, N. (1997). Scaling of microstructural parameters: Misorientations of deformed induced boundaries. *Acta Materialia*, *45*(1), 105–112.
Karato, S., Paterson, M. S., & Fitz Gerald, J. D. (1986). Rheology of synthetic olivine aggregates: Influence of grain-size and water. *Journal of Geophysical Research: Solid Earth*, *91*(B8), 8151–8176. https://doi.org/10.1029/JB091iB08p08151
Karato, S., & Wu, P. (1993). Rheology of the upper mantle: A synthesis. *Science*, *260*(5109), 771–778.
Keller, R. R., & Geiss, R. H. (2012). Transmission EBSD from 10 nm domains in a scanning electron microscope. *Journal of Microscopy*, *245*, 245–251.
Komabayashi, T., Hirose, K., Nagaya, Y., Sugimura, E., & Ohishi, Y. (2010). High temperature compression of ferropericlase and the effect of temperature on iron spin transition. *Earth and Planetary Science Letters*, *297*(3–4), 691–699.
Mainprice, D., Tommasi, A., Ferré, D., Carrez, P., & Cordier, P. (2008). Predicted glide systems and crystal preferred orientation of polycrystalline silicate Mg-Perovskite at high pressure: Implications for the seismic anisotropy in the lower mantle. *Earth and Planetary Science Letters*, *271*(1–4), 135–144.
Mao, H. K., Hemley, R. J., Fei, Y., Shu, J. F., Chen, L. C., Jephcoat, A. P., et al. (1991). Effect of pressure, temperature and composition on lattice parameters and density of $(Fe,Mg)SiO_3$-perovskite to 30 GPa. *Journal of Geophysical Research: Solid Earth*, *96*(B5), 8069–8079. https://doi.org/10.1029/91JB00176
Mariani, E., Mecklenburgh, J., Wheeler, J., Prior, D. J., & Heidelbach, F. (2009). Microstructure evolution and recrystallization during creep of MgO single crystals. *Acta Materialia*, *57*, 1886–1898.
Marquardt, K., De Graef, M., Singh, S., Marquardt, H., Rosenthal, A., & Koizuimi, S. (2017). Quantitative electron backscatter diffraction (EBSD) data analyses using the dictionary indexing (DI) approach: Overcoming indexing difficulties on geological materials. *American Mineralogist*, *102*(9), 1843–1855.
Mei, S., & Kohlstedt, D. L. (2000). Influence of water on plastic deformation of olivine aggregates 2. Dislocation creep regime. *Journal of Geophysical Research: Solid Earth*, *105*(B9), 21471–21481. https://doi.org/10.1029/2000JB900180
Nisr, C., Ribárik, G., Ungár, T., Vaughan, G. B. M., Cordier, P., & Merkel, S. (2012). High resolution three-dimensional X-ray diffraction study of dislocations in grains of $MgGeO_3$ post-perovskite at 90 GPa. *Journal of Geophysical Research: Solid Earth*, *117*, B03201. https://doi.org/10.1029/2011JB008401
Nyilas, K., Couvy, H., Cordier, P., & Ungár, T. (2006). The dislocation structure and crystallite-size in forsterite (olivine) deformed at 1400°C by 11 GPa. *Zeitschrift für Kristallographie Supplements*, *2006*(Suppl_23_2006), 135–140.
Paterson, M. S. (1987). Problems in the extrapolation of laboratory rheological data. *Tectonophysics*, *133*(1–2), 33–43.
Ram, F., Wright, S., Singh, S., & De Graef, M. (2017). Error analysis of the crystal orientations obtained by the dictionary approach to EBSD indexing. *Ultramicroscopy*, *181*, 17–26.
Rauch, E. F., & Dupuy, L. (2005). Rapid spot diffraction patterns identification through template matching. *Archives of Metallurgy and Materials*, *50*, 87–99.
Rauch, E. F., & Véron, M. (2014). Automated crystal orientation and phase mapping in TEM. *Materials Characterization*, *98*, 1–9.
Schayes, C., Bouquerel, J., Vogt, J. B., Palleschi, F., & Zaefferer, S. (2016). A comparison of EBSD based strain indicators for the study of Fe-3Si steel subjected to cyclic loading. *Materials Characterization*, *115*, 61–70.
Singh, S., & De Graef, M. (2016). Orientation sampling for dictionary-based diffraction pattern indexing methods. *Modelling and Simulation in Materials Science and Engineering*, *159*, 81–94.
Singh, S., & De Graef, M. (2017). Dictionary indexing of electron channeling patterns. *Microscopy and Microanalysis*, *23*(1), 1–10. https://doi.org/10.1017/S1431927616012769
Suzuki, S. (2013). Features of transmission EBSD and its application. *JOM*, *65*(9), 1254–1263. https://doi.org/10.1007/s11837-013-0700-6
Tange, Y., Kuwayama, Y., Irifune, T., Funakoshi, K.-I., & Ohishi, Y. (2012). V-T equation of state of $MgSiO_3$ perovskite based on the MgO pressure scale: A comprehensive reference for mineralogy of the lower mantle. *Journal of Geophysical Research: Solid Earth*, *117*, B06201. https://doi.org/10.1029/2011JB008988
Trimby, P. W. (2012). Orientation mapping of nanostructured materials using transmission Kikuchi diffraction in the scanning electron microscope. *Ultramicroscopy*, *120*, 16–24.
Tschauner, O., Ma, C., Beckett, J. R., Prescher, C., Prakapenka, V. B., & Rossman, G. R. (2014). Discovery of bridgmanite, the most abundant mineral in Earth, in a shocked meteorite. *Science*, *346*(6213), 1100–1102.
Tsujino, N., Nishihara, Y., Yamazaki, D., Seto, Y., Higo, Y., & Takahashi, E. (2016). Mantle dynamics inferred from the crystallographic preferred orientation of bridgmanite. *Nature*, *539*(7627), 81–85.
Wang, Y., Guyot, F., & Liebermann, R. C. (1992). Electron microscopy of (Mg, Fe)SiO3 Perovskite: Evidence for structural phase transitions and implications for the lower mantle. *Journal of Geophysical Research: Solid Earth*, *97*(B9), 12327–12347. https://doi.org/10.1029/92JB00870
Wenk, H.-R., Armann, M., Burlini, L., Kunze, K., & Bortolotti, M. (2009). Large strain shearing of halite: Experimental and theoretical evidence for dynamic texture changes. *Earth and Planetary Science Letters*, *280*(1–4), 205–210. https://doi.org/10.1016/j.epsl.2009.01.0
Wright, S. I., Nowell, M. M., & Field, D. P. (2011). A review of strain analysis using electron backscatter diffraction. *Microscopy and Microanalysis*, *17*(3), 316–329.
Zhong, Y., Yin, F., Sakaguchi, T., Nagai, K., & Yang, K. (2007). Dislocation structure evolution and characterization in the compression deformed Mn–Cu alloy. *Acta Materialia*, *55*(8), 2747–2756.